Chemical Engineering Journal 521 (2025) 166963

Contents lists available at ScienceDirect

Chemical Engineering Journal

journal homepage: www.elsevier.com/locate/cej

Comprehensively-upgraded polymer electrolytes with lithium ion-conductive nanosheets towards stable lithium metal batteries

Lehao Liu, Tianrong Yang, Rongmin Zhou, Rubing Xu, Jiaxin Tu, Qian Zhao, Dingrong Long, Meicheng Li *

State Key Laboratory of Alternate Electrical Power System with Renewable Energy Sources, School of New Energy, North China Electric Power University, Beijing 102206, China

ARTICLE INFO

Keywords:
Polymer electrolyte
Functionalized silica nanosheet
Ionic liquid
Lithium metal battery

ABSTRACT

Solid polymer electrolytes employing poly(ethylene oxide) (PEO) matrices have drawn extensive research focus, owing to the cost-effectiveness and high flexibility; however, their practical implementation in lithium metal batteries (LMBs) remains constrained by limited room-temperature ionic conductivity, inadequate mechanical robustness, and lithium dendrite growth. To address these challenges, Li^+-containing ionic liquids (LiILs) are confined within carboxyl-functionalized porous silica nanosheets (NSCs) to obtain active nanofillers (LiIL@NSCs) with rapid Li^+ transport channels, and then a comprehensively-upgraded composite polymer electrolyte (PL-LiIL@NSC) is prepared by integrating the active nanofillers in PEO-LiTFSI electrolyte. Benefiting from the introduction of the fast-ion pathways in the active nanofillers, and the suppression of polymer matrix crystallization and acceleration of lithium bis(trifluoromethanesulfonyl)imide (LiTFSI) decomposition by the hydrogen bond interaction between the carboxyl groups on the LiIL@NSCs and the ether oxygen groups of PEO and the $TFSI^-$ anions, the composite electrolyte shows a room-temperature ionic conductivity of 7.1×10^{-4} S cm^{-1} and a Li^+ transference number of 0.629, which are 26.3 and 3.7 times higher than the unmodified electrolyte, respectively. Meanwhile, the Young's modulus and electrochemical window increase from 34.9 MPa and 3.95 V to 104.0 MPa and 4.80 V, respectively, due to the incorporation of the active nanofillers. Thus, the Li||Li cell with the PL-LiIL@NSC composite electrolyte demonstrates stable cycling at 30 °C for 1600 h, which is 8 times longer than the pristine electrolyte-based cell. Moreover, the PL-LiIL@NSC electrolyte-based LMBs display exceptional electrochemical performance. This study offers a rational structure design strategy of composite electrolyte with Li^+-conductive nanofillers for high-stability LMBs.

1. Introduction

Lithium-ion batteries (LIBs) possess obvious merits regarding energy density and absence of memory effect, driving their widespread adoption in portable electronics, transportation systems, and power stations [1–4]. Poly(ethylene oxide) (PEO)-based solid-state electrolytes have gained prominence as viable options for lithium metal batteries (LMBs) thanks to their exceptional flexibility and favorable interfacial compatibility with metal anodes [5]. Nevertheless, the inherently low ionic conductivity severely impedes their practical application at ambient temperatures [6,7]. Additionally, the solid polymer electrolytes show inadequate mechanical robustness, insufficient oxidation stability, and they are easily penetrated due to the dendrite growth [8–11]. Consequently, the comprehensibly-ungraded polymer electrolytes featuring enhanced room-temperature ionic conductivity, elevated oxidation resistance, and reinforced mechanical integrity has become imperative for advancing practical implementation in solid-state LMBs [12].

Introducing inorganic nanoparticles into polymer matrices can inhibit polymer crystallization and promote lithium salt dissociation [13]. Studies indicated that uniformly dispersed nanofillers in solid polymer electrolytes would create continuous ion transport networks along their surface, which significantly improve the ionic conductivity [14–16]. Nonetheless, it is difficult for the polymer electrolytes to achieve room-temperature ionic conductivity exceeding the critical threshold of 0.1 mS cm^{-1} by filling inert or active inorganic nanoparticles for practical implementation [5], because of the insufficient ion transport channels within the nanofillers. It is important to exploit Li^+-

* Corresponding author.
E-mail address: mcli@ncepu.edu.cn (M. Li).

https://doi.org/10.1016/j.cej.2025.166963
Received 31 May 2025; Received in revised form 27 July 2025; Accepted 7 August 2025
Available online 8 August 2025

conductive nanofillers with fast-ion pathways for high-conductivity polymer electrolytes.

Ionic liquids (ILs) have inherent advantages over conventional organic solvents, such as non-flammability, negligible volatility and high ionic conductivity, and thus they are considered as viable additives for polymer electrolyte modification [17,18]. When integrated with PEO matrices, ILs would promote lithium salt dissociation efficiency and optimize Li^+ migration kinetics through enhanced solvent effect [19]. Nevertheless, IL-contained polymer electrolytes exhibit compromised mechanical rigidity [19,20], inferior high-voltage cathode tolerance and the side reactions in electrolyte/electrode interface [21]. To address these limitations, it is important to design a functionalized porous nanofiller to confine high-conductivity ILs without leakage for comprehensively-ungraded polymer electrolytes.

Herein, we develop a high-performance composite polymer electrolyte by filling a novel Li^+-conductive nanosheets (denoted as LiIL@NSCs) in PEO-LiTFSI electrolytes (Fig. 1). The LiIL@NSCs are prepared by confining LiTFSI-containing 1-ethyl-3-methylimidazolium bis(trifluoromethanesulfonyl)imide (EMIMTFSI) ILs (denoted as LiILs) in carboxyl-functionalized porous silica nanosheets (denoted as NSCs) through hydrogen bonding, electrostatic interactions and capillary forces, which would prevent the leakage of ILs and their side reactions with electrodes. The LiILs confined within NSCs establish fast-ion pathways, effectively boosting the ionic conductivity of the electrolytes. Meanwhile, the hydrogen bond interaction between the carboxyl groups of the LiIL@NSCs and the ether groups of PEO can disrupt the crystallization of polymer matrix, thus accelerating the PEO segment mobility and increasing the ionic conductivity. Furthermore, the selective anion coordination through the hydrogen bonding between LiIL@NSCs and $TFSI^-$ anions promotes salt dissociation efficiency, which elevates both free Li^+ concentration and Li^+ transference number while synergistically improving overall conductivity. The mechanical robustness and the high-voltage tolerance are also greatly strengthened, owing to the hydrogen bonding between the LiIL@NSCs and polymer electrolyte matrix. Therefore, the resulting composite polymer electrolyte of PEO-LiTFSI-LiIL@NSC (denoted as PL-LiIL@NSC) shows greatly improved resistance against lithium dendrite growth, and the PL-LiIL@NSC electrolyte-based solid-state LMBs demonstrate excellent electrochemical performance.

2. Experimental section

2.1. Synthesis of NSCs

The preparation of NSCs from vermiculite was performed by two steps of exfoliation and modification (Fig. S1) (Supporting Information). To exfoliate the vermiculite natural mineral, 10 g of vermiculite natural mineral after ball milling was dispersed into 1 L of saturated sodium chloride (NaCl) solution with agitation at 110 °C for 24 h. The solid phase of the mixture was isolated and subsequently purified with water to remove residual NaCl by centrifugation. The sample obtained by centrifugation was placed into 1 L of 2 M lithium chloride (LiCl) solution with agitation at 110 °C for 24 h. The solid phase of the mixture solution was isolated by centrifugation and rinsed six times in water to wash away the excessive LiCl. The sample obtained by centrifugation was placed into 100 mL of HCl with continuous agitation for 12 h at 80 °C. The solid phase of the mixture was isolated by centrifugation and then rinsed with water until neutral pH. After repeating the above process, the liquid supernatant was freeze-dried to obtain hydroxy-functionalized porous silica nanosheets (denoted as NSOs).

The functionalization of amino groups commenced with ultrasonic dispersion of NSOs in toluene, followed by the incorporation of triethylamine and aminopropyl triethoxysilane (APTES) and reflux for 24 h at 90 °C. The synthesized product was subjected to centrifugation and then rinsed with anhydrous ethanol and water, respectively. The liquid supernatant was freeze-dried to obtain amino-functionalized porous silica nanosheets (denoted as NSNs). NSNs were dispersed in of *N*, *N*-dimethylformamide (DMF), subsequently incorporated with maleic anhydride. The mixture solution was refluxed for 24 h at 90 °C. Afterward, the resultant was centrifuged, and the solid phase was separated and rinsed three times with DMF. The liquid supernatant was freeze-dried to obtain NSCs.

2.2. Preparation of LiIL@NSCs

As shown in Fig. S1, the synthesis of LiILs involved dissolving LiTFSI in EMIMTFSI (1:1.37 by weight) under continuous 40 °C agitation for 24 h, with subsequent vacuum dehydration for 2 h at 120 °C to evaporate residual moisture. The LiILs and NSCs were mixed at various mass ratios (0.25:1, 0.5:1, 1:1, 1.25:1, 1.5:1, and 2:1) and homogenized through mortar grinding for over 10 min. The composite was subsequently degassed at a vacuum oven of 80 °C to evacuate entrapped air within the NSC pores and meanwhile to facilitate the penetration of LiILs. After 12 h of vacuum treatment, the ionic liquid-impregnated NSCs were obtained. The optimized composite was designated as LiIL@NSCs (more details in Section 3.1).

2.3. Preparation of composite electrolytes

The additives (NSCs, LiILs and LiIL@NSCs) with various mass

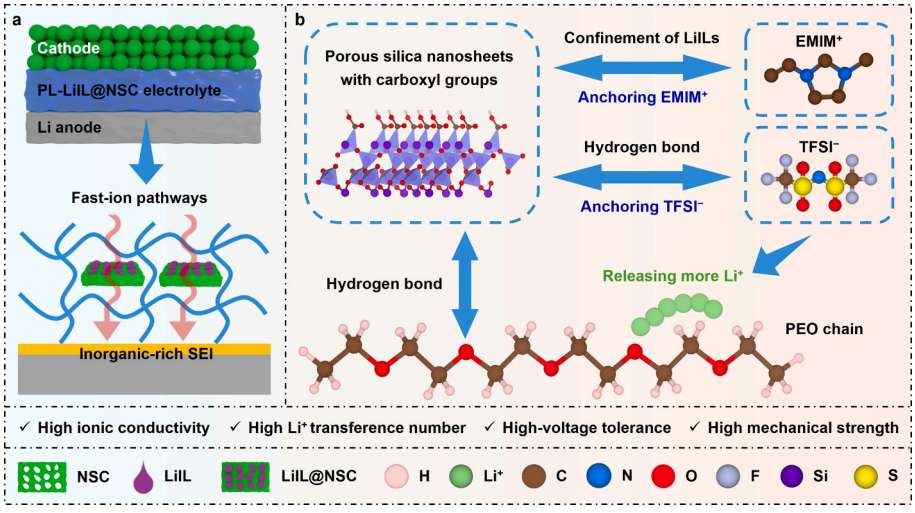

Fig. 1. Schematic illustration showing (a) the electrolyte membrane texture and (b) the role of LiIL@NSCs in PEO-LiTFSI electrolyte.

underwent dispersion in DMF via ultrasonication for 1 h and agitation for 24 h. Meanwhile, PEO (M_w = 600,000) and LiTFSI (EO:Li^+ = 18:1) were put in DMF and vigorously agitated for 24 h to obtain the homogenic polymer electrolyte precursor solution. The additive dispersion was subsequently blended with the polymer electrolyte solution and stirring for 24 h. The resulting mixed solution were subject to solution cast into Teflon molds and thermally dried under vacuum for solvent evaporation. The pristine PEO-LiTFSI electrolyte without additives was denoted as PL, while the PEO-LiTFSI electrolytes containing NSCs, LiILs, NSCs and LiILs, and LiIL@NSCs were denoted as PL-NSCm, PL-LiILm, PL-NSCm-LiILn, and PL-LiIL@NSCm, respectively (m and n represented the mass ratio of the additives). A LiIL-glass fiber (GF) composite electrolyte was also prepared by filling glass fiber separators with LiILs for comparison.

2.4. Material characterizations

Materials were measured by using scanning electron microscopy (SEM), nitrogen physisorption analysis (BET/BJH methods), X-ray diffraction (XRD), Fourier-transform infrared (FTIR) spectroscopy combined with Raman spectroscopy, tensile testing, thermogravimetric analysis (TGA), and X-ray photoelectron spectroscopy (XPS). Detailed description of the material characterization methods, please refer to Text S1.

2.5. Electrochemical measurements

Electrochemical characterizations included electrochemical impedance spectroscopy (EIS) for ionic conductivity measurement, chronoamperometry combined with EIS for Li^+ transference number (τ_{Li+}) calculation, linear sweep voltammetry (LSV) for high-voltage tolerance assessment, critical current density (CCD) and exchange current density (ECD) testing, and galvanostatic cycling of lithium metal cells. For a comprehensive description of the electrochemical characterization methods, please refer to Text S2.

3. Results and discussion

3.1. Physicochemical characterizations of LiIL@NSCs

The LiIL@NSCs remained individually separated and freely flowable when the LiIL:NSC weight ratios were 0.25:1, 0.5:1, 1:1, and 1.25:1 (Fig. 2a). However, when the LiIL:NSC weight ratio increased to 1.5:1 and 2:1, the LiIL@NSCs agglomerated severely. This was attributed to the excess viscous LiILs on the NSC surface (not entirely filled in the pores of the NSCs) and the strong adhesion of the NSCs. To avoid the severe agglomeration of the NSCs and the leakage of the LiILs in polymer electrolytes, the LiIL@NSCs with a LiIL:NSC weight ratio of 1.25:1 was chosen as Li^+-conductive nanofillers for further composite electrolyte preparation.

The LiIL-GF composite electrolyte shows a room-temperature ionic conductivity of 1.2 × 10^{-4} S cm^{-1} (Fig. S2), indicating the high ionic conductivity of LiILs. The impact of the LiIL:NSC weight ratio on the conductivity of the LiIL@NSC-based pellets was then investigated. The LiIL@NSC pellets with LiIL:NSC ratios of 0.25:1, 0.5:1, 1:1, and 1.25:1 exhibited the conductivities of 7.5 × 10^{-5}, 1.1 × 10^{-4}, 1.5 × 10^{-4}, and 3.8 × 10^{-4} S cm^{-1} at 30 °C (Fig. 2b), respectively, demonstrating a positive correlation between the LiIL proportion and the conductivity. The LiILs acted as fast-ion pathways in the NSCs, and thus increasing the ionic conductivity of the LiIL@NSC pellets. Notably, all the samples had reduced ionic conductivities at 50 °C, because of the enhanced fluidity of the LiILs in the NSC pores. As the operation temperature elevated from 50 to 80 °C, the conductivity of the LiIL@NSC pellets increased again. Although the cold-pressed LiIL@NSC pellets are studied as electrolytes, there are a few problems such as inferior flexibility, poor interfacial contact with electrodes, and large thickness. To address these issues, the LiIL@NSCs were utilized as active fillers to fabricate the polymer electrolytes with Li^+-conductive nanosheets in this study.

To probe structural evolution before and after incorporation of LiILs, the NSCs and the LiIL@NSCs were investigated by SEM, BET and FT-IR. SEM images (Fig. 2c–d) revealed similar morphology of the two samples (typical lamellar structures). BET surface characterization (Fig. 2e) revealed distinct pore architectures between the two materials. The LiIL@NSCs manifested a Langmuir-type (Type II) adsorption profile typical of low-porosity substances. In contrast, the NSCs exhibited overlapping adsorption-desorption branches at low pressures P/P_0 = 0.45–0.85 signaling microporous lamellar ordering, and a characteristic Type IV isotherm with H3 hysteresis at higher pressures (P/P_0 = 0.45–0.85) indicating mesoporous structures [22]. Moreover, the NSCs had a specific surface area of 284.2 m^2 g^{-1}, featuring a broad mesopore distribution (0–20 nm). In comparison, the LiIL@NSCs had drastically a reduced surface area (13.0 m^2 g^{-1}) with a narrow pore size distribution (0–5 nm), likely arising from interparticle stacking voids. These structural changes confirmed the effective filling of LiILs in the NSC pores, facilitating Li^+ transport in the LiIL@NSCs.

The pyrolysis behavior of the nanosheets was investigated through TGA analyses (Fig. 2f). The pristine NSCs exhibited a three-stage thermal decomposition profile: (1) an initial mass reduction of 3.6 wt% observed from 30 to 130 °C, reflecting evaporation of physically adsorbed moisture; (2) a gradual linear mass loss of 2.3 wt% at 130–240 °C,

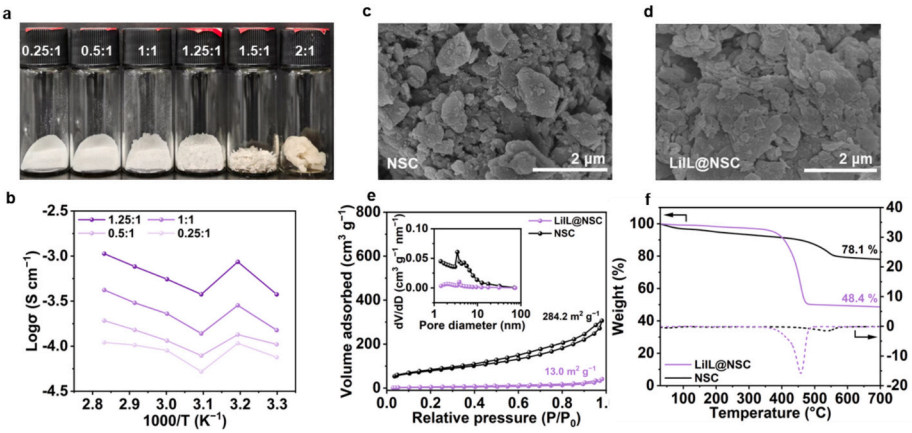

Fig. 2. Characterizations of NSCs and LiIL@NSCs. (a) Optical photographs of LiIL@NSCs with different LiIL:NSC weight ratios. (b) Ionic conductivity of LiIL@NSC pellets at 30–80 °C. SEM images of (c) NSCs and (d) LiIL@NSCs. (e) N_2 adsorption-desorption isotherms of NSCs and LiIL@NSCs, and the insets correspond to their pore distribution. (f) TGA curves of NSCs and LiIL@NSCs.

corresponding to the dehydration of carboxylic groups into anhydrides [23]; and (3) a 12.4 % mass reduction from 390 to 600 °C, arising from the synergistic pyrolysis of grafted APTES ligands and anhydrides [24]. Above 600 °C, the TGA curve became stabilized, confirming complete decomposition of organic components. As for the LiIL@NSCs, a 3.6 wt% mass loss appeared below 350 °C, ascribed to solvent evaporation and anhydride formation. Notably, despite the high LiTFSI content in the LiIL@NSCs, no mass loss related to the LiTFSI decomposition was detected between 135 and 200 °C [25]. Subsequent mass loss at 350–480 °C was related to the disintegration of the LiILs [26]. The characterization results indicated the successful LiIL infusion within the pores of the NSCs and the formation of fast-ion pathways within the LiIL@NSCs.

3.2. Morphology of electrolytes

Polymer electrolytes were obtained by a solution casting approach followed by a solvent evaporation process (Fig. 3a). When the LiIL@NSC content exceeded 20 wt%, the PL-LiIL@NSC electrolyte membranes were tightly adhered on Teflon molds, leading to structural fragmentation during peeling (Fig. S3). Thus, the maximum allowable content of LiIL@NSCs was 20 wt%. An investigation was then conducted to evaluate the concentration-dependent performance of LiIL@NSC additives in polymer electrolytes, focusing on three critical parameters of ionic conductivity, high-voltage cathode compatibility, and mechanical properties. As delineated in Supplementary Fig. S4, the PL-LiIL@NSC electrolytes demonstrated progressive enhancement in ionic conductivity with increasing additive loading, reaching a maximum value at 20 wt% incorporation (PL-LiIL@NSC20). The oxidization stability and mechanical strength was also enhanced with the LiIL@NSC addition (Figs. S5 and S6). Therefore, the PL-LiIL@NSC20 electrolyte was selected for further investigation. Besides, to investigate the role of multiple components in the PL-LiIL@NSC20 electrolyte, a series of electrolytes of PL, PL-NSC9, PL-LiIL11, and PL-NSC9-LiIL11 were also prepared.

The surface morphology of electrolytes was determined via SEM (Fig. 3b–f). The pristine PL electrolyte membrane had numerous cracks and pores (Fig. 3b). The incorporation of NSCs significantly reduced these defects (Fig. 3c). However, the agglomeration of NSCs was observed in the PL-NSC9 electrolyte with a high nanofiller content of 9 wt%, which would cause high interfacial impedance at the electrode/electrolyte interfaces. The addition of LiILs to PL and PL-NSC9 electrolytes (for PL-LiIL11 and PL-NSC9-LiIL11) increased the defect density (Fig. 3d–e), due to the plasticizing effect of LiILs, which would compromise mechanical strength. In contrast, the PL-LiIL@NSC20 electrolyte had minimal cracks or pores (Fig. 3f), because LiILs were primarily confined in the NSC pores.

3.3. Ionic conductivity of electrolytes

The influence of additive components on Li^+ transportation in electrolyte was first investigated through ionic conductivity (Fig. 4a). The unmodified PL electrolyte displayed a limited ionic conductivity of 2.7×10^{-5} S cm^{-1} at 30 °C. Introducing 9 wt% NSCs enhanced ion transport behavior, yielding an elevated conductivity of 5.5×10^{-5} S cm^{-1} for the PL-NSC9 electrolyte. The incorporation of LiILs in the PL and PL-NSC9 electrolytes furtherly increased the conductivities to 1.1×10^{-4} and 3.0×10^{-4} S cm^{-1} for the PL-LiIL11 and PL-NSC9-LiIL11 electrolytes, respectively. The most substantial enhancement emerged from the addition of LiIL@NSCs, where the PL-LiIL@NSC20 electrolyte achieved a conductivity of 7.1×10^{-4} S cm^{-1}, which demonstrated 26.3 and 2.4 times higher than the PL and PL-NSC9-LiIL11 electrolytes, respectively, attributing to the fast-ion pathways in the LiIL@NSCs.

Arrhenius fitting analyses were utilized to quantify Li^+ transport barriers (Fig. 4a). The activation energy (E_a) decreased slightly from 0.79 eV (the pristine PL electrolyte) to 0.78 eV (PL-NSC9 electrolyte),

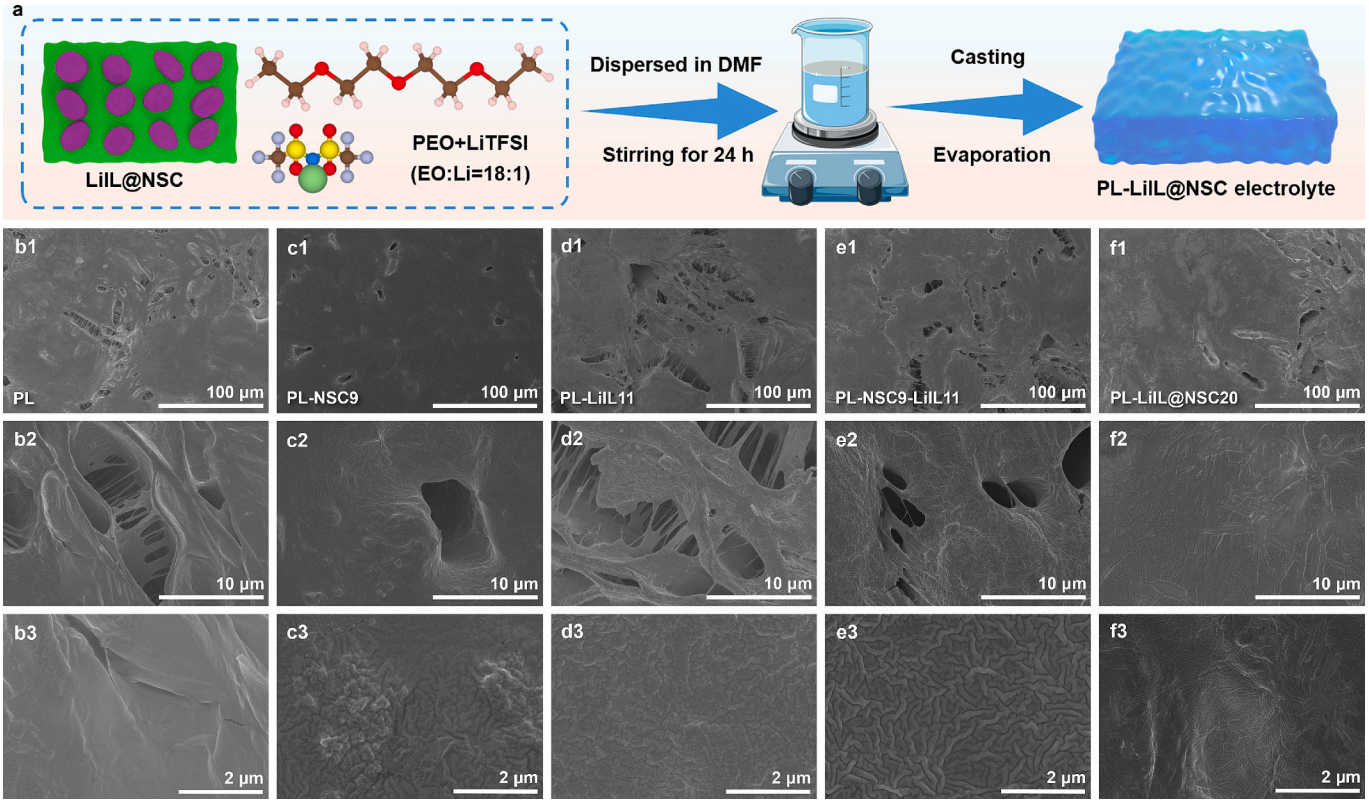

Fig. 3. (a) Schematic illustration of fabrication of PL-LiIL@NSC electrolytes. SEM images of (b1 – b3) PL, (c1 – c3) PL-NSC9, (d1 – d3) PL-LiIL11, (e1 – e3) PL-NSC9-LiIL11, and (f1 – f3) PL-LiIL@NSC20 electrolyte surfaces.

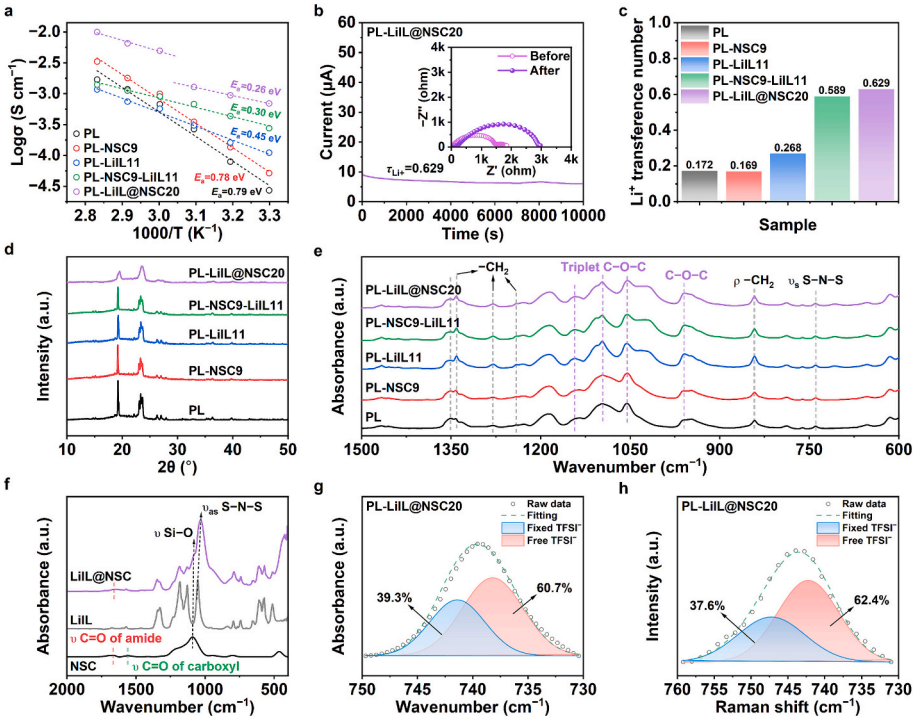

Fig. 4. Electrical properties. (a) Arrhenius plots of PL, PL-NSC9, PL-LiIL11, PL-NSC9-LiIL11 and PL-LiIL@NSC20 electrolytes. (b) Chronoamperometry profile of Li||Li cell with PL-LiIL@NSC20 electrolyte, and the insets correspond to its electrochemical impedance pre- and post-polarization. (c) Calculation results of Li^+ transference numbers. (d) XRD patterns of PL, PL-NSC9, PL-LiIL11, PL-NSC9-LiIL11 and PL-LiIL@NSC20 electrolytes. (e) FT-IR spectra of PL, PL-NSC9, PL-LiIL11, PL-NSC9-LiIL11 and PL-LiIL@NSC20 electrolytes. (f) FT-IR spectra of NSCs, LiILs and LiIL@NSCs. (g) FT-IR spectra and (h) Raman spectra of PL-LiIL@NSC20 electrolyte fitted with Gaussian−Lorentzian.

because of the incorporation of NSCs. The E_a values further decreased to 0.45 eV (PL-LiIL11 electrolyte) and 0.30 eV (PL-NSC9-LiIL11 electrolyte), due to the addition of LiILs [27]. Moreover, the PL-LiIL@NSC20 electrolyte had the lowest E_a value (0.26 eV), consistent with the ionic conductivity. These results demonstrated that pore-confined LiILs in NSCs functioned as fast-ion pathways to lower the energy barrier in the composite electrolyte. The reason for the E_a value decrease by the LiIL@NSC addition will be discussed in the following parts.

The τ_{Li+} of the electrolytes was systematically evaluated (Fig. 4b−c and Fig. S7). The pristine PL electrolyte exhibited a low τ_{Li+} value of 0.172. The PL-NSC9 electrolyte also showed a similar τ_{Li+} value of 0.169, due to the NSC agglomeration in the electrolyte. Incorporation of LiILs into the PL electrolyte caused increase of the τ_{Li+} value to 0.268 (PL-LiIL11 electrolyte) and 0.589 (PL-NSC9-LiIL11 electrolyte). Due to the confinement of LiILs in the NSC pores and the hydrogen bond interaction between the carboxyl groups of NSCs and the $TFSI^-$, the PL-LiIL@NSC20 electrolyte showed the highest τ_{Li+} value of 0.629, which was 3.7 times higher than the PL electrolyte. This elevated τ_{Li+} value would be helpful for mitigating the space charge accumulation, reducing electrochemical polarization during cycling, and suppressing dendrite growth [28,29].

The structural evolution of electrolytes was investigated by XRD (Fig. 4d). All the electrolytes exhibited characteristic diffraction peaks at 19° and 23°, which were identified as the (120) and (112) crystallographic planes of PEO, respectively [30]. Compared to the pristine PL electrolyte, the PL-NSC9 electrolyte showed slightly reduced peak intensities, suggesting the suppression of PEO crystallinity by the NSCs. The incorporation of LiILs further weakened the peak intensities of the PL-LiIL11 and PL-NSC9-LiIL11 electrolytes, indicating the disrupted PEO chain ordering due to plasticizing effect of LiILs. The peak intensities of the PL-LiIL@NSC20 electrolyte were the lowest, indicating the lowest PEO crystallinity of the electrolyte. DSC tests further revealed that the PL-NSC9-LiIL11 and PL-LiIL@NSC20 electrolytes had much lower crystallinities of 31.8 % and 29.9 % than the PL electrolyte (40.9 %), respectively (Fig. S8). The low crystallinity would facilitate the PEO segment mobility and promote Li^+ transportation in electrolyte. Thus, the PL-LiIL@NSC20 electrolyte showed the highest ionic conductivity and the lowest activation energy (Fig. 4a).

The interactions of NSCs, LiILs and LiIL@NSCs with the electrolyte matrix were analyzed using FT-IR spectroscopy (Fig. 4e and Table S1). First, the effect of these components on PEO were investigated. Compared to the LiIL-free electrolyte, the PL-LiIL11, PL-NSC9-LiIL and PL-LiIL@NSC20 electrolytes exhibited slight shift and intensity change in the vibration peaks related to $-CH_2$ groups (near 842, 1241, 1280, 1341 and 1350 cm^{-1}) and C − O − C groups (near 960, 1055, 1096 and 1141 cm^{-1}). These phenomena can be attributed to the reduced PEO crystallinity and elevated segmental mobility induced by the incorporation of EMIMTFSI and LiTFSI. Furthermore, the C − O − C peaks of the PL electrolyte at 961.8, 1055.4, and 1143.1 cm^{-1} shifted in both the PL-NSC9-LiIL11 (958.4, 1054.8 and 1142.6 cm^{-1}) and PL-LiIL@NSC20 (958.8, 1054.3 and 1141.7 cm^{-1}) electrolytes, which should be attributed to the hydrogen bond interaction between the carboxyl groups of NSCs and the ether oxygen groups of PEO. This was also conducive to disrupting the orderly arrangement of the PEO segments and furtherly reducing the crystallinity of the polymer matrix (Fig. 4d and Fig. S8).

In order to clarify the interactions and chemical bonds between NSCs and $TFSI^-$ anions, the FT-IR spectra of NSCs, LiILs and LiIL@NSCs were also measured (Fig. 4f and Table S2). The characteristic peaks at 462.1, 800.5, 1089.8, and 1222.3 cm^{-1} correspond to silica-related bonds, while the peaks at 1570.1 and 1670.4 cm^{-1} are assigned to C═O stretching vibrations of amide and carboxyl groups of the NSCs. After mixing LiILs and NSCs, the obtained LiIL@NSCs still contain the most peaks of both NSCs and LiILs. In addition, the shift of the S − N − S asymmetric stretching vibration (from 1052.9 cm^{-1} in LiILs to 1032.7 cm^{-1} in LiIL@NSCs) provides the evidence for the formation of robust hydrogen bond interaction between $TFSI^-$ and the carboxyl groups of

NSCs, which is beneficial to increasing the dissociation efficiency of lithium salts and releasing free Li^+. Consequently, the electrical properties of the PL-NSC9-LiIL11 and PL-LiIL@NSC20 electrolytes enhanced significantly (Fig. 4a and c).

The S − N − S symmetric stretching vibration peak (~740 cm^{-1}) could be deconvoluted into two peaks related to free $TFSI^-$ anions (~738 cm^{-1}) and immobilized $TFSI^-$ anions (~742 cm^{-1}) (Fig. 4g and Fig. S9) [2,31,32]. The pristine PL electrolyte had 22.5 % anchored $TFSI^-$ anions. The anchored $TFSI^-$ anions increased to 28.5 % upon the NSC addition (PL-NSC9 electrolyte), resulting from the hydrogen bond between the carboxyl groups of NSCs and $TFSI^-$. The incorporation of LiILs would be also beneficial for anchoring the $TFSI^-$ anions through the electrostatic attraction between $EMIM^+$ cations and $TFSI^-$ anions. Thus, 29.2 % and 36.5 % $TFSI^-$ anions were immobilized in the PL-LiIL11 and PL-NSC9-LiIL11 electrolytes. Moreover, confining LiILs within the NSC pores maximized the contact area between the NSCs and the LiILs, and therefore 39.3 % $TFSI^-$ anions were anchored in the PL-LiIL@NSC20 electrolyte. The immobilization of $TFSI^-$ anions would increase the τ_{Li+} value of the electrolytes. Raman spectra (Fig. 4h and Fig. S10) further proved that the fractions of anchored $TFSI^-$ anions of the PL, PL-NSC9, PL-LiIL11, PL-NSC9-LiIL11, and PL-LiIL@NSC20 electrolytes were 19.1 %, 22.9 %, 25.8 %, 30.2 %, and 37.6 %, respectively, consistent with the FT-IR results [31,33].

In short, the enhanced ionic transport properties of the PL-LiIL@NSC20 electrolyte arisen from synergistic effects. Firstly, the hydrogen bond between the carboxyl groups of LiIL@NSCs and the ether oxygen groups of PEO chains, combined with the plasticizing effect of LiILs, inhibited the PEO crystallization and improved the polymer chain mobility. Secondly, the hydrogen bond interaction between the carboxyl groups of LiIL@NSCs and the $TFSI^-$ was beneficial for anchoring the $TFSI^-$, and elevated the dissociation efficiency of LiTFSI and the free Li^+ concentration. Thus, the activation energy was greatly reduced with the LiIL@NSC filling. The last but not least, the fast-ion pathways in the active LiIL@NSCs greatly facilitated the ion transport.

3.4. Mechanical and electrochemical properties of electrolytes

Tensile testing results (Fig. 5a–b) revealed that the pristine PL electrolyte exhibited an inferior strength of 0.61 MPa with 127 % elongation, while the incorporation of the NSCs made the ultimate tensile strength of the PL-NSC9 electrolyte elevate to 0.93 MPa, because of the hydrogen bonding between the NSCs and the electrolyte matrix. However, the addition of LiILs reduced the strengths of the PL-LiIL11 (0.46 MPa) and PL-NSC9-LiIL11 (0.53 MPa) electrolytes, due to the plasticization effect of LiILs. In contrast, the PL-LiIL@NSC20 electrolyte retained a high strength of 0.88 MPa, as LiILs were confined in the NSC pores, weakening the plasticization effect. Similarly, the PL-NSC9 and PL-LiIL@NSC20 electrolytes had high toughness of 1.52 and 0.55 MJ m^{-3} (Fig. 5c). As shown in Fig. 5d, the PL-LiIL@NSC20 electrolyte also possessed a Young's modulus of 104.0 MPa, 3.0 and 1.3 times higher than those of the PL (34.9 MPa) and PL-NSC9-LiIL11 (81.7 MPa) electrolytes, respectively. The enhanced Young's modulus would be helpful for impeding the lithium dendrite growth [34].

The high-voltage tolerance of the electrolytes was assessed by LSV tests (Fig. 5e). The unmodified PL electrolyte demonstrated a low oxidation stabilization voltage of ~3.95 V. The LiIL-GF electrolyte also

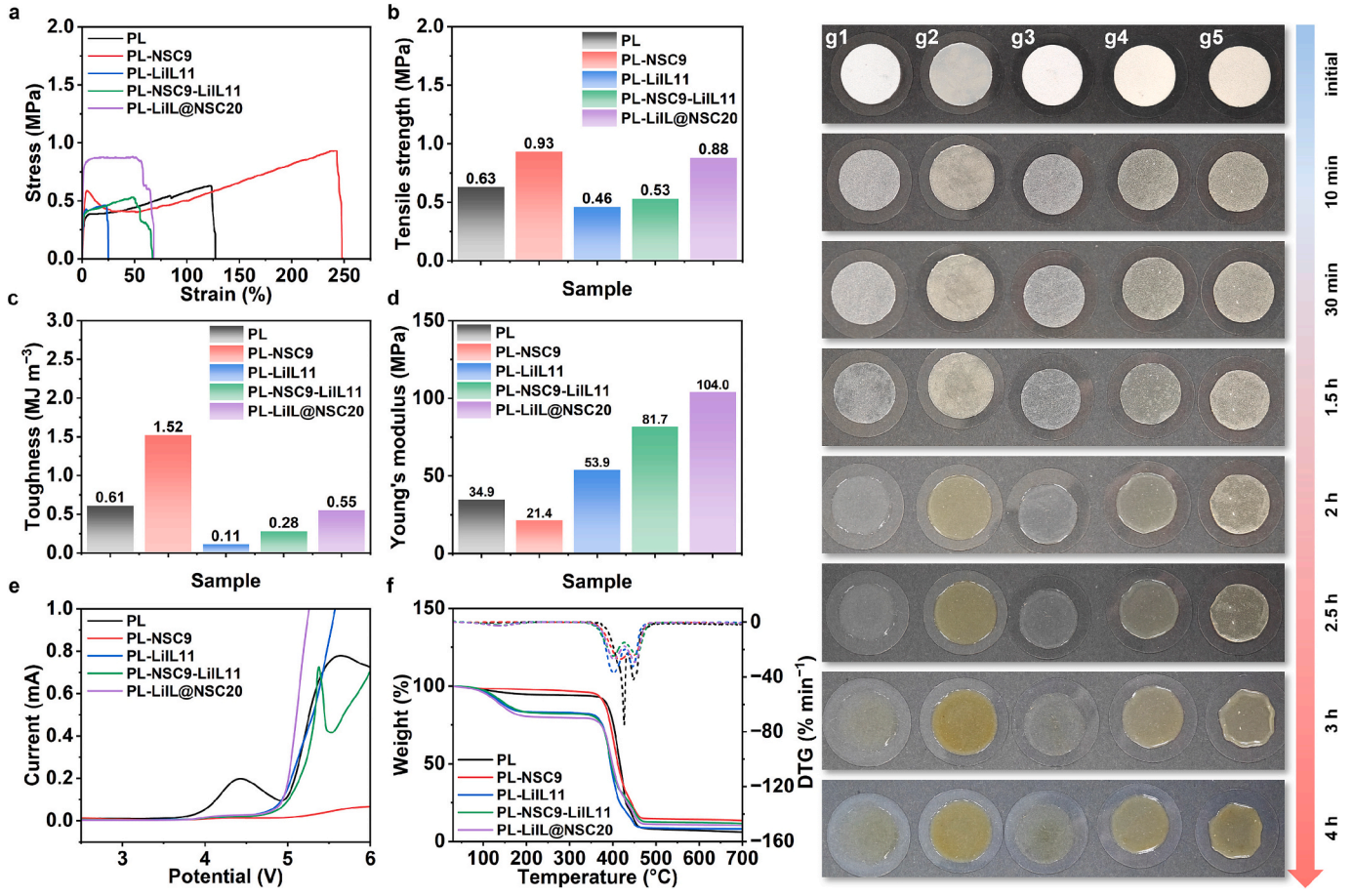

Fig. 5. Mechanical, electrochemical and thermal properties of electrolytes. (a) Stress-strain curves, (b) tensile strength, (c) toughness, (d) Young's modulus, (e) LSV curves and (f) TGA curves of PL, PL-NSC9, PL-LiIL11, PL-NSC9-LiIL11 and PL-LiIL@NSC20 electrolytes. Optical photographs of (g1) PL, (g2) PL-NSC9, (g3) PL-LiIL11, (g4) PL-NSC9-LiIL11 and (g5) PL-LiIL@NSC20 electrolytes heated at 140 °C for different time.

demonstrated a low oxidation stabilization voltage of ~3.74 V (Fig. S11). It should be mentioned that the LiIL@NSC pellets with LiIL: NSC weight ratios of less than 1.25:1 exhibited greatly improved oxidization stability. In contrast, the PL-NSC9 electrolyte demonstrated a broad electrochemical window of 5.20 V, owing to the hydrogen bond between the carboxyl groups of the NSCs and the ether oxygen atoms of PEO and the $TFSI^-$ anions (Fig. 4e–f). This would effectively suppress the oxidative decomposition of PEO and $TFSI^-$ at higher voltages. Moreover, the PL-LiIL11, PL-NSC9-LiIL11 and PL-LiIL@NSC20 electrolytes showed higher oxidation stabilization voltages of ~4.80 V, which was beneficial for their electrochemical compatibility with high-voltage cathodes [9].

The thermal decomposition behaviors of the electrolytes were detected through TGA measurements (Fig. 5f). As for the PL electrolyte, the mass loss below 135 °C was related to the evaporation of free DMF solvent, while that at 135–200 °C was primarily related to the LiTFSI decomposition [25]. Besides, a pronounced mass loss at 370–460 °C corresponded to the PEO disintegration [35]. The PL-NSC9 electrolyte

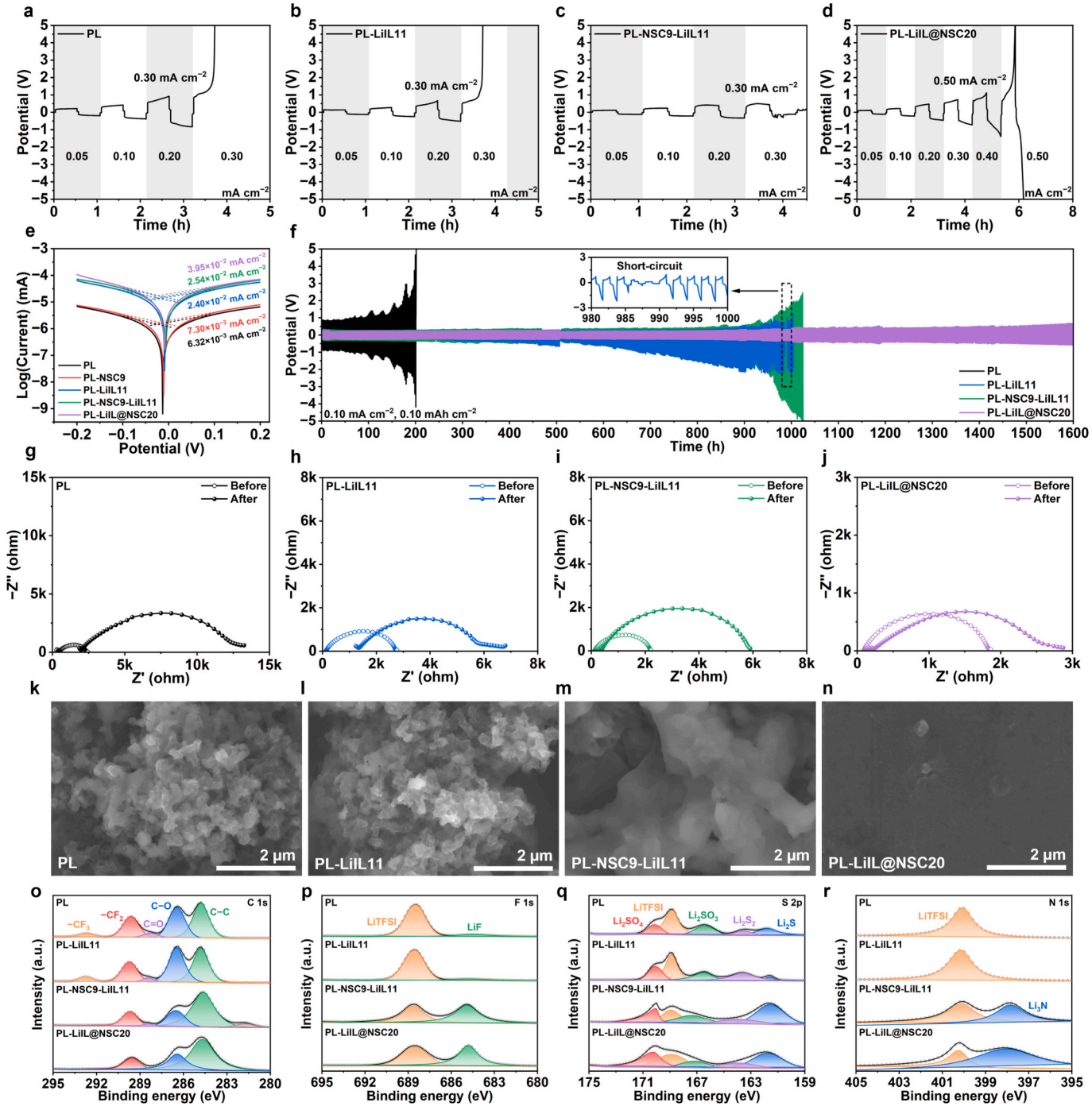

Fig. 6. Resistance against dendrites. CCD test of (a) PL, (b) PL-LiIL11, (c) PL-NSC9-LiIL11 and (d) PL-LiIL@NSC20 electrolyte-based Li||Li cells at 30 °C. (e) Tafel plots of Li||Li cells based on PL, PL-NSC9, PL-LiIL11, PL-NSC9-LiIL11 and PL-LiIL@NSC20 electrolytes. (f) Galvanostatic cycling curves of PL, PL-LiIL11, PL-NSC9-LiIL11 and PL-LiIL@NSC20 electrolyte-based Li||Li cells at 30 °C. EIS spectra of Li||Li cells based on (g) PL, (h) PL-LiIL11, (i) PL-NSC9-LiIL11 and (j) PL-LiIL@NSC20 electrolytes under pre-cycling and post-cycling conditions. Surface morphology of the cycled Li electrodes from Li||Li cells using (k) PL, (l) PL-LiIL11, (m) PL-NSC9-LiIL11 and (n) PL-LiIL@NSC20 electrolytes. High-resolution (o) C 1s, (p) F 1s, (q) S 2p, and (r) N 1s XPS spectra of the cycled Li electrodes.

exhibited similar three-stage decomposition behaviors, but it demonstrated retarded LiTFSI degradation, owing to the hydrogen bond between the NSCs and $TFSI^-$. Moreover, the PL-LiIL11, PL-NSC9-LiIL11 and PL-LiIL@NSC20 electrolytes containing 11 wt% LiILs (and higher LiTFSI content than the PL and PL-NSC9 electrolytes) displayed higher weight loss at 135–200 °C.

To verify the thermal stability, the electrolyte discs were subjected to isothermal treatment for different time (Fig. 5g). The PL, PL-LiIL11, and PL-NSC9-LiIL11 electrolyte membranes completely melted after 2 h at 140 °C, and they became from white to yellow after 3 h due to the LiTFSI decomposition, consistent with the TGA results (Fig. 5f). In contrast, the PL-LiIL@NSC20 membrane began to melt at the circular edge after 2 h, because of the confinement of LiILs in the NSC pores. In short, the incorporation of the LiIL@NSC nanofillers enhanced the mechanical robustness and high-voltage tolerance of the polymer electrolyte.

3.5. Resistance against Li dendrites of electrolytes

The CCDs of the electrolytes were measured through stepwise current ramp testing on Li||Li symmetric cells with the PL, PL-NSC9, PL-LiIL11, PL-NSC9-LiIL11, and PL-LiIL@NSC20 electrolytes at 30 °C (Fig. 6a−d and Fig. S12). The PL electrolyte-based cell exhibited a CCD of 0.30 mA cm^{-2}. After the incorporation of NSCs, the PL-NSC9 electrolyte-based cell displayed a low CCD of 0.10 mA cm^{-2}, due to inferior interfacial contact between the PL-NSC9 electrolyte membrane and lithium electrodes. The PL-LiIL11 and PL-NSC9-LiIL11 electrolyte-based cells also maintained CCD values of 0.30 mA cm^{-2}, owing to the optimized Li^+ transport kinetics and excellent interfacial electrolyte/electrode contact. Remarkably, the PL-LiIL@NSC20 electrolyte-based cell delivered a high CCD of 0.50 mA cm^{-2}, because of the greatly improved ionic transport properties and the enhanced mechanical strength (Figs. 4a−c and 5a−d).

The ECDs were then determined by Tafel polarization analyses of the Li||Li cells (Fig. 6e). Benefiting from the enhanced electrical properties, the PL-LiIL@NSC20 electrolyte-based cell showed a much higher ECD of 3.95×10^{-2} mA cm^{-2} than the PL (6.32×10^{-3} mA cm^{-2}), PL-NSC9 (7.30×10^{-3} mA cm^{-2}), PL-LiIL11 (2.40×10^{-2} mA cm^{-2}), and PL-NSC9-LiIL11 (2.54×10^{-2} mA cm^{-2}) electrolyte-based cells, implying the faster electrochemical reactions in the Li|PL-LiIL@NSC20|Li cell [31,36,37].

To assess the lithium dendrite suppression capability of the electrolytes under ambient conditions, long-term cycling tests were performed on the Li||Li cells at 30 °C (Fig. 6f and Fig. S13). When cycled at 0.10 mA cm^{-2} (areal capacity: 0.10 mAh cm^{-2}), the cell employing the PL-NSC9 electrolyte suffered from abrupt failure within 0.3 h (Fig. S13), consistent with its low CCD of 0.10 mA cm^{-2}. The PL electrolyte-based cell sustained cycling for 200 h before failure. The PL-LiIL11 electrolyte-based cell short-circuited after 985 h, and the potential greatly increased after 500 h, because of the low τ_{Li+} and mechanical strength, which induced the concentration polarization and susceptibility to dendrite growth. Owing to the improvement on electrical properties and mechanical strength, the PL-NSC9-LiIL11 and PL-LiIL@NSC20 electrolyte-based cells can work for 1024 and 1600 h, respectively. When cycled at a higher current density of 0.20 mA cm^{-2}, the PL-LiIL@NSC20 electrolyte-based cell can also work stably (Fig. S14), demonstrating superior dendrite inhibition capability and exceptional cycling stability.

EIS measurements were conducted to reveal the impedance variation of the cells (Fig. 6g−j and Fig. S15). The PL-NSC9 electrolyte-based cell exhibited a high initial interfacial resistance (R_i) of 9459 Ω (Fig. S15), indicating the poor electrode/electrolyte contact. This was the reason why the Li|PL-NSC9|Li cell showed a low CCD and a short cycling life (Figs. S12 and S13). Although the PL electrolyte-based cell showed a low initial R_i value of 2084 Ω, its R_i value soon increased to 11,023 Ω in 200 h (Fig. 6g). Due to the enhancement of ion conductance, the PL-LiIL11 electrolyte-based cell displayed a low R_i value of 5387 Ω after 985 h (Fig. 6h). The PL-NSC9-LiIL11 electrolyte-based cell also displayed lower R_i values of 2103 and 5519 Ω before and after 1024 h, respectively (Fig. 6i), due to the synergistic improvement in ion transport and mechanical toughness. Notably, the cell utilizing the PL-LiIL@NSC20 electrolyte showed the lowest R_i of 1780 and 2599 Ω before and after 1600 h, respectively (Fig. 6j).

SEM characterizations were then performed to disclose the dendrite situation of the electrochemically-cycled cells. There were a lot of dendrites on the cycled lithium electrodes coupled with the PL and PL-LiIL11 electrolytes (Fig. 6k−l). This resulted in the elevation of the resistance and potential and the short-circuit failure of the cells (Fig. 6f−h). Although there were no dendrites on the lithium electrode coupled with the PL-NSC9-LiIL11 electrolyte, there were a few pores on the lithium electrode and the surface was relatively rough (Fig. 6m), because of the uneven lithium stripping and deposition. In stark contrast, there were a few sparse granular lithium deposits on the lithium electrode coupled with the PL-LiIL@NSC20 electrolyte, indicating the greatly-enhanced lithium dendrite inhibition ability by the electrolyte (Fig. 6n).

The component of the solid-state interphase (SEI) on the cycled lithium electrodes were investigated by XPS. As revealed by the C 1 s spectra in Fig. 6o, the electrodes coupled with the PL-NSC9-LiIL11 and PL-LiIL@NSC20 electrolytes showed much lower C − O vibration-related peak intensity at ~286.5 eV than the electrodes coupled with the PL and PL-LiIL11 electrolytes. The electrodes paired with the PL-NSC9-LiIL11 and PL-LiIL@NSC20 electrolytes also showed much higher LiF-related peak intensities at ~684.7 eV (Fig. 6p). Moreover, the S 2p and N 1 s spectra revealed that the electrodes paired with the PL-NSC9-LiIL11 and PL-LiIL@NSC20 electrolytes had much higher peak intensities at ~161.6 (related to Li_2S) and ~ 397.9 eV (related to Li_3N) (Fig. 6q−r). Thus, the SEI layers of the lithium electrodes paired with the PL-NSC9-LiIL11 and PL-LiIL@NSC20 electrolytes possessed abundant inorganic components (e.g., LiF, Li_2S and Li_3N) with high mechanical modulus, surface energy or ionic conductivity, which was beneficial for inhibiting the dendrite growth (Fig. 6f) [38,39].

3.6. Lithium metal battery performance

Rate performance tests were conducted on the LiIL-GF, PL, PL-NSC9, PL-LiIL11, PL-NSC9-LiIL11, and PL-LiIL@NSC20 electrolyte-based Li|| LFP cells at 30 °C under varying C-rates to evaluate their rate capability (Fig. 7a and Fig. S16). The PL-LiIL@NSC20-based cell exhibited superior rate performance, delivering discharge capacities of 170, 163, 154 and 100 mAh g^{-1} at 0.1, 0.2, 0.3 and 0.5C, respectively. These values significantly outperformed those of cells using LiIL-GF (126, 123 and 118 mAh g^{-1}), PL (149, 82 and 23 mAh g^{-1}), PL-NSC9 (9, 0 and 0 mAh g^{-1}), PL-LiIL11 (160, 132 and 3 mAh g^{-1}) and PL-NSC9-LiIL11 (166, 158 and 19 mAh g^{-1}) electrolytes at 0.1, 0.2 and 0.3C. Notably, after 25 rate-cycling iterations and subsequent reversion to 0.1C, the cell utilizing the PL-LiIL@NSC20 electrolyte retained a high capacity of 164 mAh g^{-1}, surpassing the capacities of LiIL-GF (123 mAh g^{-1}), PL (146 mAh g^{-1}), PL-NSC9 (11 mAh g^{-1}), PL-LiIL11 (156 mAh g^{-1}) and PL-NSC9-LiIL11 (161 mAh g^{-1}) electrolyte-based cells. Furthermore, the charge-discharge profiles of the PL-LiIL@NSC20-based cell consistently displayed narrow voltage plateaus across all tested rates, indicative of lower electrochemical polarization compared to other electrolyte systems (Fig. S17).

Long-term cycling stability tests were further conducted on Li||LFP cells at 30 °C under 0.3C (Fig. 7b, Figs. S18 and 19). The cell employing the LiIL-GF electrolyte delivered an initial capacity of 105 mAh g^{-1}, and retained 83 mAh g^{-1} after 73 cycles (78 % capacity retention) (Fig. S18). The cell employing the PL-NSC9 electrolyte sustained discharge capacities below 20 mAh g^{-1} throughout testing, demonstrating fundamental incompatibility with operational requirements. The cell employing the PL electrolyte delivered an initial capacity of 74 mAh g^{-1}, yet experienced rapid deterioration to 45 mAh g^{-1} within 33 cycles (61 % retention). Conversely, the PL-LiIL@NSC20 electrolyte-based cell

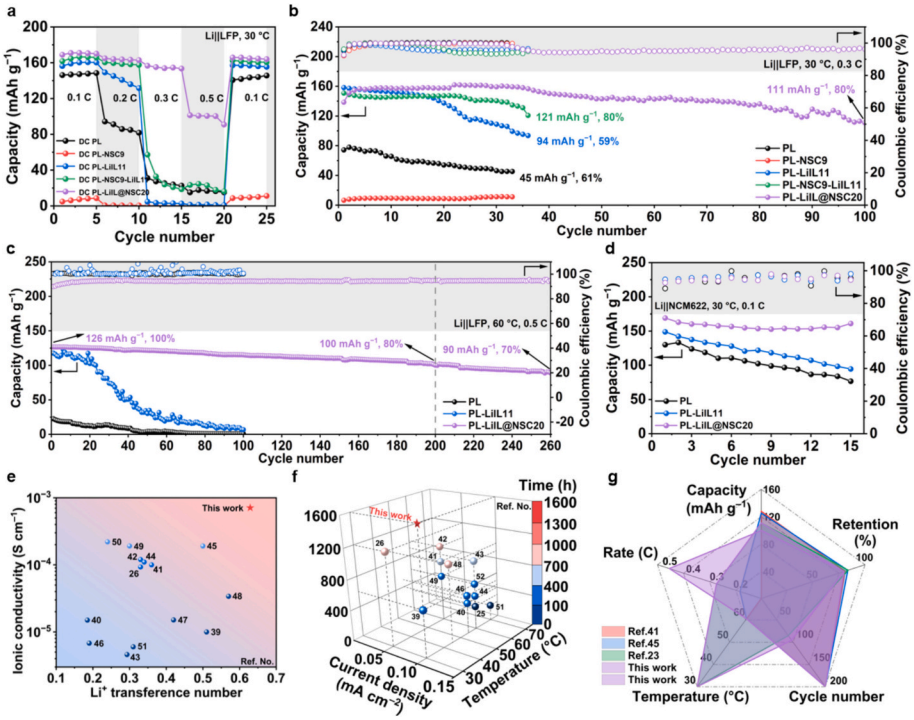

Fig. 7. Electrochemical performance of lithium metal cells. (a) Rate performance of Li||LFP cells based on the PL, PL-NSC9, PL-LiIL11, PL-NSC9-LiIL11 and PL-LiIL@NSC20 electrolytes at 30 °C. Cycling performance of Li||LFP cells (b) at 30 °C and 0.3C, and (c) at 60 °C and 0.5C. (d) Cycling performance of Li||NCM622 cells at 30 °C and 0.1C. Comparison of (e) electrical properties of electrolytes, (f) Li||Li cell performance, and (g) Li||LFP cell performance recently reported in open literatures [25,26,39–52]. More details are given in Table S3.

achieved exceptional long-term cycling stability, achieving an initial capacity of 139 mAh g^{-1} and retaining 111 mAh g^{-1} after 100 cycles (80 % retention), significantly outperforming the cells with the LiIL-GF, PL, PL-LiIL11 (94 mAh g^{-1} at 36th cycle, 59 % retention) and PL-NSC9-LiIL11 (121 mAh g^{-1} at 36th cycle, 80 % retention) electrolytes.

To assess electrolyte viability under high-temperature condition, long-term cycling stability assessments were conducted using Li||LFP cells at 60 °C under 0.5C (Fig. 7c and Fig. S20). The cell employing the baseline PL electrolyte sustained discharge capacities below 23 mAh g^{-1} throughout testing, failing to meet practical requirements. In contrast, the PL-LiIL@NSC20 electrolyte-based cell demonstrated superior performance, achieving an initial capacity of 126 mAh g^{-1} while retaining 100 mAh g^{-1} after 200 cycles (80 % capacity retention) and 90 mAh g^{-1} after 260 cycles (70 % capacity retention). This significantly outperformed the PL and PL-LiIL11 (7 mAh g^{-1} after 100 cycles, 6 % capacity retention) electrolyte-based cells. We also conducted rate performance tests on the Li||LFP cells at a low temperature of 20 °C (Fig. S21), and found that the PL-LiIL@NSC20 electrolyte-based cell outperformed both the PL and PL-LiIL11 electrolyte-based cells. These results furtherly demonstrate its exceptional potential for electrochemical applications across a wide temperature range.

The electrolyte/electrode interfacial stability was evaluated by comparing the EIS spectra of Li||LFP cells under pre-cycling and post-cycling conditions (Fig. S22). For the PL-LiIL@NSC20 electrolyte-based cell cycled at 30 °C under 0.3C, the charge transfer resistance (R_{ct}) increased from 560 Ω (pre-cycling) to 2102 Ω (post-cycling), which remained significantly lower than those of the PL (2503 to 8029 Ω), PL-NSC9 (7921 to 18,340 Ω), PL-LiIL11 (1849 to 2157 Ω), and PL-NSC9-LiIL11 (1961 to 2366 Ω) electrolyte-based cells, indicating the enhanced electrolyte/electrode interface stability by the PL-LiIL@NSC20 electrolyte.

To investigate the performance of the PL-LiIL@NSC20 electrolytes in high-voltage lithium metal batteries, galvanostatic rate capability assessments were performed on the Li||NCM622 cells within 2.8–4.2 V at 30 °C under varying C-rates (Fig. S23). The cell employing the baseline PL electrolyte demonstrated severely limited rate capacities of 112, 16 and 0 mAh g^{-1} at 0.1, 0.2 and 0.3C, respectively, while the PL-LiIL11 electrolyte-based cell showed marginally improved capacities of 95, 30 and 3 mAh g^{-1} under identical testing conditions. Conversely, the Li|PL-LiIL@NSC20|NCM622 cell had significantly enhanced electrochemical performance with high reversible capacities of 184, 83 and 23 mAh g^{-1} at corresponding C-rates, with capacity recovery to 154 mAh g^{-1} upon returning to 0.1C. The PL-LiIL@NSC20 electrolyte-based cell charged to a high voltage of 4.5 V still exhibited excellent rate capability (Fig. S24). Furthermore, the prolonged cycling evaluations revealed the superior stability of the PL-LiIL@NSC20 electrolyte-based cells, maintaining 166 mAh g^{-1} after 15 cycles (99 % capacity retention from initial capacity of 167 mAh g^{-1}), which substantially exceeded the performance of the PL (77 mAh g^{-1}, 60 % capacity retention) and PL-NSC9-LiIL11 electrolyte-based cells (95 mAh g^{-1}, 63 % capacity retention) (Fig. 7d and Fig. S25).

Comprehensive comparison of the electrical and electrochemical performance of PL-LiIL@NSC20 electrolyte against existing literatures reveals the critical advancements of this work (Fig. 7e–g and Table S3). With the superior electrical properties, the PL-LiIL@NSC20 electrolyte surpasses those of other PEO-based solid-state electrolytes (Fig. 7e). The Li||Li cell cycle stability at 0.10 mA cm^{-2} (areal capacity: 0.10 mAh cm^{-2}) is also higher than the previous reports (Fig. 7f). Notably, while most published PEO-based solid-state LMBs exhibit operational limitations at ambient temperature, the PL-LiIL@NSC20 electrolyte-based Li||LFP cell demonstrates superior electrochemical properties at both 30 and 60 °C (Fig. 7g). Combined with the exceptional electrochemical performance observed in Li||NCM622 cell configurations (Fig. 7d, and Figs. S23–25), these results collectively suggest that the PL-LiIL@NSC20 electrolyte holds significant potential for practical applications.

4. Conclusions

In summary, this work developed Li^+-conductive LiIL@NSCs by confining LiILs within the porous structure of NSCs, effectively mitigating leakage-induced side reactions of LiILs. Benefiting from the hydrogen bonding between the carboxyl groups and the ether groups of PEO and the $TFSI^-$ of LiTFSI, synergizing with the plasticizing effect of LiILs, the LiIL@NSCs effectively impeded the PEO crystallization and facilitated the LiTFSI decomposition, thus resulting in the great enhancement in ionic conductivity (7.1×10^{-4} vs. 2.7×10^{-5} S cm^{-1} at 30 °C), Li^+ transference number (0.629 vs. 0.172), mechanical strength, thermal stability and oxidization stabilization potential (4.80 vs. 3.95 V) of polymer electrolytes. Moreover, the LiIL@NSC-containing composite electrolyte demonstrated improved lithium dendrite suppression, evidenced by enhanced CCD (0.50 vs. 0.30 mA cm^{-2}) and ECD (3.95×10^{-2} vs. 6.32×10^{-3} mA cm^{-2}), enabling Li||Li cells to achieve prolonged cycling (1600 vs. 200 h). The composite electrolyte-based Li|| LFP cathodes delivered 80 % capacity retention after 100 cycles at 30 °C and 0.3C and 80 % capacity retention after 200 cycles at 60 °C and 0.5C with high capacities. Additionally, the Li||NCM622 cells exhibited improved electrochemical performance, demonstrating practical potential for solid-state LMBs. This study offered a novel road to fabricate comprehensively-enhanced polymer electrolytes with fast-ion pathways for high-stability LMBs.

CRediT authorship contribution statement

Lehao Liu: Writing – review & editing, Writing – original draft, Visualization, Validation, Supervision, Software, Resources, Project administration, Methodology, Investigation, Funding acquisition, Formal analysis, Data curation, Conceptualization. **Tianrong Yang:** Visualization, Validation, Supervision, Software, Methodology, Investigation, Formal analysis, Data curation. **Rongmin Zhou:** Supervision, Software, Formal analysis. **Rubing Xu:** Supervision, Software, Formal analysis. **Jiaxin Tu:** Visualization, Software. **Qian Zhao:** Writing – review & editing, Supervision, Methodology. **Dingrong Long:** Visualization, Methodology, Formal analysis. **Meicheng Li:** Writing – review & editing, Writing – original draft, Visualization, Validation, Supervision, Software, Resources, Project administration, Methodology, Investigation, Funding acquisition, Formal analysis, Data curation, Conceptualization.

Declaration of competing interest

The authors declare that they have no known competing financial interests or personal relationships that could have appeared to influence the work reported in this paper.

Acknowledgments

This work is supported partially by project of National Natural Science Foundation of China (52272200, 52302250), Hebei Natural Science Foundation (E2022502022), the project of China Three Gorges Corporation named key technologies of intelligent joint regulation and operation with grid connected friendly in power station group of wind, solar photovoltaic and energy storage (WWKY-2021-0173), Huaneng Group Headquarters Science and Technology Project (HNKJ20-H88), the Fundamental Research Funds for the Central Universities (2025MS040), and the NCEPU "Double First-Class" Program.

Appendix A. Supplementary data

Supplementary data to this article can be found online at https://doi.org/10.1016/j.cej.2025.166963.

Data availability

Data will be made available on request.

References

[1] L. Liu, M. Li, L. Chu, B. Jiang, R. Lin, X. Zhu, G. Cao, Layered ternary metal oxides: performance degradation mechanisms as cathodes, and design strategies for high-performance batteries, Prog. Mater. Sci. 111 (2020) 100655.
[2] M. Xu, S. Liang, H. Shi, J. Miao, F. Tian, W. Cui, R. Shao, Z. Xu, High-strength MOF-based polymer electrolytes with uniform ionic flow for lithium dendrite suppression, Small 20 (2024) 2406007.
[3] D. Zhang, X. Meng, W. Zhang, J. Mo, Q. Zhao, B. Wang, Q. Fan, L. Liu, T. Yang, Y. Jin, R. Zhou, M. Zhang, M. Li, A thin and ultrahigh-ionic-conductivity composite electrolyte with 3D aramid nanofiber networks toward ambient-temperature lithium metal batteries, Adv. Energy Mater. 15 (2025) 2403565.
[4] L. Wang, S. Xu, Z. Wang, E. Yang, W. Jiang, S. Zhang, X. Jian, F. Hu, A nano fiber–gel composite electrolyte with high Li+ transference number for application in quasi-solid batteries, eScience 3 (2023) 100090.
[5] Y. Su, F. Xu, X. Zhang, Y. Qiu, H. Wang, Rational design of high-performance PEO/ceramic composite solid electrolytes for lithium metal batteries, Nano-Micro Letters 15 (2023) 82.
[6] K. Khan, M.B. Hanif, H. Xin, A. Hussain, H.G. Ali, B. Fu, Z. Fang, M. Motola, Z. Xu, M. Wu, PEO-based solid composite polymer electrolyte for high capacity retention all-solid-state lithium metal battery, Small 20 (2024) 2305772.
[7] L. Liu, R. Xu, J. Tu, R. Zhou, J. Mo, T. Yang, Q. Zhao, M. Zhang, D. Zhang, M. Li, Thin polymer electrolytes with 3D nanofiber skeletons enabling high-performance solid-state lithium metal batteries, J. Phys. Chem. C 129 (2025) 6138–6147.
[8] M.S. Su'ait, A. Ahmad, H. Hamzah, M.Y.A. Rahman, Preparation and characterization of PMMA−MG49−$LiClO_4$ solid polymeric electrolyte, J. Phys. D. Appl. Phys. 42 (2009) 055410.
[9] H. An, M. Li, Q. Liu, Y. Song, J. Liu, Z. Yu, X. Liu, B. Deng, J. Wang, Strong Lewis-acid coordinated PEO electrolyte achieves 4.8 V-class all-solid-state batteries over 580 Wh kg^{-1}, Nat. Commun. 15 (2024) 9150.
[10] L. Liu, J. Lyu, J. Mo, H. Yan, L. Xu, P. Peng, J. Li, B. Jiang, L. Chu, M. Li, Comprehensively-upgraded polymer electrolytes by multifunctional aramid nanofibers for stable all-solid-state Li-ion batteries, Nano Energy 69 (2020) 104398.
[11] Z. Wu, S. He, C. Zheng, J. Gan, L. She, M. Zhang, Y. Gao, Y. Yang, H. Pan, Fabrication pressures and stack pressures in solid-state battery, eScience 4 (2024) (2024) 100247.
[12] T. Yi, E. Zhao, Y. He, T. Liang, H. Wang, Quantification and visualization of spatial distribution of dendrites in solid polymer electrolytes, eScience 4 (2024) 100182.
[13] V. Vijayakumar, M. Ghosh, K. Asokan, S.B. Sukumaran, S. Kurungot, J. Mindemark, D. Brandell, M. Winter, J.R. Nair, 2D layered nanomaterials as fillers in polymer composite electrolytes for lithium batteries, Adv. Energy Mater. 13 (2023) 2203326.
[14] J. Zheng, Y.-Y. Hu, New insights into the compositional dependence of Li-ion transport in polymer–ceramic composite electrolytes, ACS Appl. Mater. Interfaces 10 (2018) 4113–4120.
[15] N. Wu, P.-H. Chien, Y. Li, A. Dolocan, H. Xu, B. Xu, N.S. Grundish, H. Jin, Y.-Y. Hu, J.B. Goodenough, Fast Li^+ conduction mechanism and interfacial chemistry of a NASICON/polymer composite electrolyte, J. Am. Chem. Soc. 142 (2020) 2497–2505.
[16] L. Liu, J. Mo, R. Zhou, T. Yang, R. Xu, J. Tu, Q. Zhao, M. Zhang, D. Zhang, B. Wang, D. Long, K. Yang, J. Zhang, M. Li, Ultrathin solid composite electrolytes for long-life lithium metal batteries, J Energy Storage 114 (2025) 115777.
[17] Y. Yoshida, K. Fujie, D.-W. Lim, R. Ikeda, H. Kitagawa, Superionic conduction over a wide temperature range in a metal−organic framework impregnated with ionic liquids, Angew. Chem. Int. Ed. 58 (2019) 10909–10913.
[18] X. Tang, S. Lv, K. Jiang, G. Zhou, X. Liu, Recent development of ionic liquid-based electrolytes in lithium-ion batteries, J. Power Sources 542 (2022) 231792.
[19] Z. Zhang, Y. Huang, H. Gao, C. Li, J. Huang, P. Liu, 3D glass fiber cloth reinforced polymer electrolyte for solid-state lithium metal batteries, J. Membr. Sci. 621 (2021) 118940.
[20] D. Yu, Z. Ma, Z. Liu, X. Jiang, H.A. Younus, X. Wang, S. Zhang, Optimizing interfacial wetting by ionic liquid for high performance solid-state lithium metal batteries operated at ambient temperature, Chem. Eng. J. 457 (2023) 141043.
[21] Z. Lei, J. Shen, J. Wang, Q. Qiu, G. Zhang, S.-S. Chi, H. Xu, S. Li, W. Zhang, Y. Zhao, Y. Deng, C. Wang, Composite polymer electrolytes with uniform distribution of ionic liquid-grafted ZIF-90 nanofillers for high-performance solid-state Li batteries, Chem. Eng. J. 412 (2021) 128733.
[22] W.-Y. Li, Z.-H. Luo, X. Long, J.-Y. Long, C. Pang, H. Li, X. Zhi, B. Shi, J.-J. Shao, Y.-B. He, Cation vacancy-boosted Lewis acid–base interactions in a polymer electrolyte for high-performance lithium metal batteries, ACS Appl. Mater. Interfaces 13 (2021) 51107–51116.
[23] L. Yang, C. Fan, J. Zhang, F. Zhang, R. Li, S. Yi, Y. Sun, H. Dong, Poly(acrylic acid)-modified silica nanoparticles as a nonmetal catalyst for $NaBH_4$ methanolysis, Int. J. Hydrog. Energy 46 (2021) 23236–23244.
[24] Z. Wang, L. Ouyang, H. Li, L. Wågberg, M.M. Hamedi, Layer-by-layer assembly of strong thin films with high lithium ion conductance for batteries and beyond, Small 17 (2021) 2100954.
[25] L. Liu, D. Zhang, T. Yang, W. Hu, X. Meng, J. Mo, W. Hou, Q. Fan, K. Liu, B. Jiang, L. Chu, M. Li, Flexible ion-conducting membranes with 3D continuous nanohybrid

networks for high-performance solid-state metallic lithium batteries, J. Energy Chem. 75 (2022) 360–368.
[26] F. Li, B. Zhou, J. He, H. Zhou, C. Meng, X. Li, Y. Shen, X. Tao, W. Kong, H. Chen, A. Yuan, Polyethylene oxide-based solid electrolytes with fast Li-ion transport channels constructed from 2D montmorillonite for solid-state lithium-metal batteries, Chem. Eng. J. 488 (2024) 150700.
[27] L. Tian, Y. Liu, Z. Su, Y. Cao, W. Zhang, S. Yi, Y. Zhang, B. Niu, P. Dong, D. Long, A lithiated organic nanofiber-reinforced composite polymer electrolyte enabling Li-ion conduction highways for solid-state lithium metal batteries, J. Mater. Chem. A 9 (2021) 23882–23890.
[28] X. Meng, D. Zhang, J. Mo, L. Liu, T. Yang, Q. Fan, Q. Zhao, R. Zhou, M. Zhang, W. Hou, W. Hu, W. Zhang, Y. Jin, B. Jiang, L. Chu, M. Li, Room-temperature solid-state metallic lithium batteries based on high-content boron nitride nanosheet-modified polymer electrolytes, Appl. Surf. Sci. 648 (2024) 158962.
[29] Q. Wang, J.-F. Wu, Z.-Y. Yu, X. Guo, Composite polymer electrolytes reinforced by two-dimensional layer-double-hydroxide nanosheets for dendrite-free lithium batteries, Solid State Ionics 347 (2020) 115275.
[30] Y. Cheng, Z. Cai, J. Xu, Z. Sun, X. Wu, J. Han, Y.-H. Wang, M.-S. Wang, Zwitterionic cellulose-based polymer electrolyte enabled by aqueous solution casting for high-performance solid-state batteries, Angew. Chem. Int. Ed. 63 (2024) e202400477.
[31] K. Liu, H. Cheng, Z. Wang, Y. Zhao, Y. Lv, L. Shi, X. Cai, Z. Cheng, H. Zhang, S. Yuan, A 3 μm-utrathin hybrid electrolyte membrane with integrative architecture for all-solid-state lithium metal batteries, Adv. Energy Mater. 14 (2024) 2303940.
[32] Y. Wei, T.-H. Liu, W. Zhou, H. Cheng, X. Liu, J. Kong, Y. Shen, H. Xu, Y. Huang, Enabling all-solid-state Li metal batteries operated at 30 °C by molecular regulation of polymer electrolyte, Adv. Energy Mater. 13 (2023) 2203547.
[33] H. Li, Z. Ao, Y. Wan, Y. Liang, P. Li, Y. Zou, PEO kaolinite intercalation interface accelerates lithium-ion transfer for all-solid-state lithium metal batteries, Electrochim. Acta 507 (2024) 145011.
[34] M. Wang, C. Wang, Z. Fan, G. Wu, L. Liu, Y. Huang, Aramid nanofiber-based porous membrane for suppressing dendrite growth of metal-ion batteries with enhanced electrochemistry performance, Chem. Eng. J. 426 (2021) 131924.
[35] S. Suriyakumar, S. Gopi, M. Kathiresan, S. Bose, E.B. Gowd, J.R. Nair, N. Angulakshmi, G. Meligrana, F. Bella, C. Gerbaldi, A.M. Stephan, Metal organic framework laden poly(ethylene oxide) based composite electrolytes for all-solid-state Li-S and Li-metal polymer batteries, Electrochim. Acta 285 (2018) 355–364.
[36] C. He, H. Ying, L. Cai, H. Chen, Z. Xu, S. Liu, P. Huang, H. Zhang, W. Song, J. Zhang, L. Shi, W. Gao, D. Li, W.-Q. Han, Tailoring stable PEO-based electrolyte/electrodes interfaces via molecular coordination regulating enables 4.5 V solid-state lithium metal batteries, Adv. Funct. Mater. 34 (2024) 2410350.
[37] X. Wang, D. Pan, L. Xu, D. Mo, H. Xie, Y. Meng, K. Deng, Fluorine and carbonate regulated nonflammable polymer electrolyte for ultrastable high-voltage Li metal batteries, Energy Storage Mater 76 (2025) 104129.
[38] T. Li, X.-Q. Zhang, P. Shi, Q. Zhang, Fluorinated solid-electrolyte interphase in high-voltage lithium metal batteries, Joule 3 (2019) 2647–2661.
[39] X. Da, J. Chen, Y. Qin, J. Zhao, X. Jia, Y. Zhao, X. Deng, Y. Li, N. Gao, Y. Su, Q. Rong, X. Kong, J. Xiong, X. Hu, S. Ding, G. Gao, CO_2-assisted induced self-assembled aramid nanofiber aerogel composite solid polymer electrolyte for all-solid-state lithium-metal batteries, Adv. Energy Mater. 14 (2024) 2303527.
[40] E. Zhao, Y. Guo, Y. Liu, S. Liu, G. Xu, Nanostructured zeolitic imidazolate framework-67 reinforced poly(ethylene oxide) composite electrolytes for all solid state Lithium ion batteries, Appl. Surf. Sci. 573 (2022) 151489.
[41] C. Li, Y. Huang, C. Chen, X. Feng, Z. Zhang, High-performance polymer electrolyte membrane modified with isocyanate-grafted Ti^{3+} doped TiO_2 nanowires for lithium batteries, Appl. Surf. Sci. 563 (2021) 150248.
[42] C. Li, Y. Huang, X. Feng, Z. Zhang, H. Gao, J. Huang, Silica-assisted cross-linked polymer electrolyte membrane with high electrochemical stability for lithium-ion batteries, J. Colloid Interface Sci. 594 (2021) 1–8.
[43] Y. Li, Y. Qin, J. Zhao, M. Ma, M. Zhang, P. Li, S. Lu, H. Bu, K. Xi, Y. Su, S. Ding, Boosting the ion mobility in solid polymer electrolytes using hollow polymer nanospheres as an additive, ACS Appl. Mater. Interfaces 14 (2022) 18360–18372.
[44] Q. Guo, F. Xu, L. Shen, Z. Wang, J. Wang, H. He, X. Yao, Poly(ethylene glycol) brush on $Li_{6.4}La_3Zr_{1.4}Ta_{0.6}O_{12}$ towards intimate interfacial compatibility in composite polymer electrolyte for flexible all-solid-state lithium metal batteries, J. Power Sources 498 (2021) 229934.
[45] Z. Zhang, Y. Huang, H. Gao, C. Li, J. Hang, P. Liu, MOF-derived multifunctional filler reinforced polymer electrolyte for solid-state lithium batteries, J. Energy Chem. 60 (2021) 259–271.
[46] E. Zhao, Y. Guo, A. Zhang, H. Wang, G. Xu, Polydopamine coated TiO_2 nanofiber fillers for polyethylene oxide hybrid electrolytes for efficient and durable all solid state lithium ion batteries, Nanoscale 14 (2022) 890–897.
[47] J. Wen, Q. Zhao, X. Jiang, G. Ji, C. Xu, Graphene oxide enabled flexible PEO-based solid polymer electrolyte for all-solid-state lithium metal battery, ACS Appl. Energy Mater. 4 (2021) 3660–3669.
[48] Z. Yang, Z. Sun, C. Liu, Y. Li, G. Zhou, S. Zuo, J. Wang, W. Wu, Lithiated nanosheets hybridized solid polymer electrolyte to construct Li^+ conduction highways for advanced all-solid-state lithium battery, J. Power Sources 484 (2021) 229287.
[49] C. Li, Y. Huang, C. Chen, X. Feng, Z. Zhang, P. Liu, A high-performance solid electrolyte assisted with hybrid biomaterials for lithium metal batteries, J. Colloid Interface Sci. 608 (2022) 313–321.
[50] J.A. Isaac, L.R. Mangani, D. Devaux, R. Bouchet, Electrochemical impedance spectroscopy of PEO-LATP model multilayers: ionic charge transport and transfer, ACS Appl. Mater. Interfaces 14 (2022) 13158–13168.
[51] X. Yin, L. Wang, Y. Kim, N. Ding, J. Kong, D. Safanama, Y. Zheng, J. Xu, D.V. M. Repaka, K. Hippalgaonkar, S.W. Lee, S. Adams, G.W. Zheng, Thermal conductive 2D boron nitride for high-performance all-solid-state lithium–sulfur batteries, Adv. Sci. 7 (2020) 2001303.
[52] L. Han, J. Wang, X. Mu, T. Wu, C. Liao, N. Wu, W. Xing, L. Song, Y. Kan, Y. Hu, Controllable magnetic field aligned sepiolite nanowires for high ionic conductivity and high safety PEO solid polymer electrolytes, J. Colloid Interface Sci. 585 (2021) 596–604.